

# Spin-to-charge conversion driven by inverse chiral-induced spin selectivity

Tian-Yi Zhang<sup>1</sup>, Peng-Yi Liu<sup>1</sup>, Ai-Min Guo<sup>2</sup>, & Qing-Feng Sun<sup>1,3\*</sup>

<sup>1</sup>International Center for Quantum Materials, School of Physics, Peking University, Beijing, 100871, China

<sup>2</sup>Hunan Key Laboratory for Super-microstructure and Ultrafast Process, School of Physics, Central South University, Changsha 410083, China

<sup>3</sup>Hefei National Laboratory, Hefei 230088, China

\*Correspondence author: Qing-Feng Sun

Email: [sunqf@pku.edu.cn](mailto:sunqf@pku.edu.cn)

**Author Contributions:** Q.S. designed research; Q.S. supervised the research; T.Z. performed research; T.Z. analyzed data; and T.Z., P.L., A.G., and Q.S. wrote the paper.

**Competing Interest Statement:** The authors declare no conflict of interest.

**This PDF file includes:**

Main Text  
Figures 1 to 4

## Abstract

Chiral molecules have attracted significant multidisciplinary interest and extensive research owing to their remarkable ability to achieve charge-to-spin conversion, known as the chiral-induced spin selectivity (CISS). A recent experiment has revealed that chiral molecules also exhibit an unexpected capability for spin-to-charge conversion, referred to as the inverse CISS (ICISS), opening unprecedented avenues for the study and application of chiral molecules. Here, we propose a specific theoretical explanation, suggesting that ICISS arises from the spin-dependent deflection of electrons caused by the interaction between the spin and chiral structure. Our numerical results are in excellent agreement with experimental observations, demonstrating that ICISS persists under strong disorder. Our model also reproduces the inverse spin Hall effect (ISHE) in this experiment. Comparative analysis reveals that ICISS employs an unconventional spin-to-charge conversion mechanism distinct from conventional ISHE approaches. We provide a comprehensive explanation of ICISS, elucidate experimental phenomena, and pave the way for organic-based spintronics.

## Main Text

### Introduction

Spintronics, a vibrant interdisciplinary field bridging physics, chemistry, and biology, has received significant attention through its manipulation of electron spin, an intrinsic quantum property alongside charge (1). A central challenge in spintronics is achieving fast and low-power reversible conversion between charge current and spin current, which is crucial for the effective manipulation and control of spin-based devices (1, 2). Conventional approaches utilizing the spin Hall effect (SHE) (3, 4) and inverse spin Hall effect (ISHE) (5, 6) have established a feasible framework where charge current  $J_c$  and spin current  $J_s$  become interconvertible in non-magnetic materials. The SHE generates a transverse spin current from a charge current  $J_s \propto J_c \times \sigma_s$ , while its reciprocal ISHE produces a transverse charge current from a spin current  $J_c \propto J_s \times \sigma_s$ , with  $\sigma_s$  denoting spin polarization direction. This mutual conversion mechanism has enabled both material characterization (4) and device implementation (7) in modern spintronics. However, SHE and ISHE rely on the material's small spin Hall angle (typically only a few percent), exhibit a relatively short spin diffusion length, and are limited in terms of material systems (4). Most critically, they lack diverse means to control the spin-charge conversion process. Therefore, developing alternative, efficient, and highly tunable mechanisms for spin-charge conversion becomes imperative.

Emerging as a paradigm-shifting alternative, the chiral-induced spin selectivity (CISS) effect in organic molecules (8–10) introduces a highly promising direction to spin control. Chirality, the geometric property where an object cannot be superimposed onto its mirror image by rotations or

translations, has been shown to be intrinsically linked to electron spin in organic molecules (11). When a spin-unpolarized charge current  $J_c$  passes through chiral molecules, it becomes spin-polarized current, with its polarization direction either parallel or antiparallel to the molecular chiral axis, depending on the molecular chirality (11, 12). First observed in photoemission experiments with stearyl lysine (8), the CISS has since been robustly confirmed in diverse chiral materials, including DNA (9, 13, 14), proteins (15), and other organic systems (11, 16–18). Meanwhile, numerous theories have been proposed to explain CISS (19–25), with spin-orbit coupling (SOC) generally acknowledged as playing a key role in the spin-selective process (19–21, 25, 26). These experimental and theoretical achievements all demonstrate that CISS holds tremendous research and application prospects (11, 16, 27–29).

This CISS effect, enabling charge-to-spin conversion akin to SHE, raises a fundamental question: does its reciprocal effect, the inverse CISS (ICISS), exist? ICISS promises revolutionary chirality-mediated spin-to-charge conversion, potentially unlocking unprecedented paradigms for molecular spintronics. However, despite CISS being found for decades, experimental observation of ICISS in organic molecules has only recently been achieved (30). In this groundbreaking experiment, Sun *et al.* used a solution printing method to fabricate thin films of chiral assembled  $\pi$ -conjugated polymers (30, 31). By employing ferromagnetic resonance as a spin pump, a pure spin current  $J_s$  was injected perpendicularly into the polymer film plane. The spin polarization direction  $\sigma_s$  was oriented in-plane and parallel to the polymer chiral axis  $\Omega_{R/S}$  (right- and left-handed polymers are denoted as R or S, respectively) (30). Two distinct voltage probe configurations were used to measure the resulting charge currents: one oriented perpendicular to  $\sigma_s$  to detect the ISHE signal  $V_{ISHE}$ , and another oriented parallel to  $\sigma_s$  to detect the ICISS signal  $V_{ICISS}$ . Remarkably, the sign of  $V_{ISHE}$  was independent of molecular chirality, but  $V_{ICISS}$  reversed upon changing the molecular chirality. When  $\sigma_s$  was switched from parallel to perpendicular (still in-plane) to  $\Omega_{R/S}$ , a finite  $V_{ISHE}$  (measuring perpendicular to  $\sigma_s$ ) persisted while  $V_{ICISS}$  (measuring parallel to  $\sigma_s$ ) became nearly undetectable. This landmark experiment provides an ideal platform for investigating the interplay between molecular chirality and diverse spin conversion phenomena (30). However, the theoretical origin of the ICISS observed in this system remains unclear, underscoring an urgent need for further theoretical elucidation.

In this work, we investigate the transport properties of chiral molecular systems identical to the experiment (30), and present a comprehensive theoretical framework that elucidates the origins of both ISHE and ICISS. We demonstrate that both the ISHE and ICISS originate from SOC within the system, with ICISS arising from the combined effect of the chiral structure and SOC. This combined effect breaks the symmetry of electron motion for different spins along the chiral axis  $\Omega_{R/S}$ , resulting in spin-to-charge conversion along  $\Omega_{R/S}$ . By constructing a theoretical model, we

numerically reproduce all experimental observations including ISHE and ICISS, and show their persistence even under strong disorder. We also find a fundamental distinction between the ISHE and ICISS: while the charge current in ISHE follows the relation  $J_c \propto J_s \times \sigma_s$ , the charge current in ICISS exhibits  $J_c \propto \Omega_{R/S}$ . Our work unveils the microscopic origin of ICISS and establishes chiral molecules as a transformative platform for spin conversion, paving the way for advances in organic spintronics.

## Results

**Physical picture of spin current injection and the ISHE/ICISS.** We first construct a theoretical model corresponding to the experimental configuration (30), illustrated schematically in Fig. 1A. In Fig. 1A, the orange box region represents the spin injector layer, experimentally composed of  $\text{Ni}_{81}\text{Fe}_{19}$ . Directly beneath this layer (along the  $-x$  direction), the purple box region denotes the chiral molecular layer. This layer consists of an assembly of chiral polymers, each possessing a chiral structure (30, 31) (SI Appendix). The chiral molecular layer has size parameters  $L_x = 4$  ( $x$  direction thickness) and  $L_y = 25$  ( $y$  direction width), meaning there are  $L_x \times L_y$  chiral molecules. We use our previously developed model (19, 20, 23, 25), which includes SOC and chiral structures, to simulate the single chiral molecule. This model successfully accounts for the spin filtering effect in chiral molecules (20), explains the CISS effect in electron donor–chiral molecule–acceptor systems (23), and elucidates the chiral-induced spin polarization and magnetization effect in chiral molecules (25), demonstrating its robust explanatory power for CISS-related phenomena. In the chiral molecular layer, each molecule has a length  $L_z = 25$  along its chiral axis  $\Omega_{R/S}$ , which is oriented parallel to the  $z$ -axis (SI Appendix). Voltage probes are attached along both the  $y$  direction and  $z$  direction of the chiral molecular layer. These probes measure the voltage differences, denoted  $V_y$  and  $V_z$ , respectively, along these axes (SI Appendix). Note that the coordinate axis labeling here differs slightly from the experiment (30) (the  $x, y, z$  axes herein correspond to  $z, x, y$  axes in experiments, respectively). In this coordinate convention, our model Hamiltonian maintains formal consistency with prior works (19, 20, 23, 25) (SI Appendix), and the coordinate labeling does not affect physical conclusions provided that the measurement configuration remains identical to that in experiments.

Next, we simulate the spin-pumping process according to the experimental configuration (30). In the experiment, microwave radiation and an external magnetic field are applied to the spin injector layer, which drives the precession of the magnetization within it, inducing a spin accumulation at the interface between spin injector layer and the chiral molecular layer (32). Consequently, the chemical potential for electrons with spin parallel to the external field increases

by  $eV_0$ , while the chemical potential for electrons with antiparallel spin decreases by  $eV_0$  (33, 34). Here,  $e$  is the elementary charge and  $V_0$  is the equivalent voltage determined by the spin-pumping approach, which is set as the voltage unit. Consequently, as shown in the Fig. 1A, a pure spin current  $J_s$  (aligned to the  $-x$  direction) is injected to the chiral molecular layer. In Fig. 1A, the direction of spin polarization  $\sigma_s$  (marked by the blue arrow) is in the  $+z$  direction (35), meaning that the spin  $+z$  electrons are pushed into the chiral molecular layer, and the spin  $-z$  electrons are pulled out of the chiral molecular layer. Using the non-equilibrium Green's function method (36–38) (SI Appendix), under the drive of spin bias  $eV_0$  (34), the spin current  $J_s$  and the voltages  $V_y$  and  $V_z$  perpendicular to and along the direction of the molecular chiral axis  $\Omega_{R/S}$  can be calculated.

After describing the experimental spin injection configuration, we then analyze the physical origins of the ISHE and ICISS. Both ISHE and ICISS are induced by the SOC within the system. One contribution to the SOC originates from the interfacial electric field  $E_x$  at the heterojunction formed between two layers (39). This interfacial electric field  $E_x$  (perpendicular to the interface along the  $x$ -axis) (40) gives rise to Rashba-type SOC  $H_{so}^E = e\hbar/(4m_e^2c^2)[E_x \cdot (\sigma \times p)]$  (41), where  $m_e$ ,  $c$ ,  $\sigma = (\sigma_x, \sigma_y, \sigma_z)$  and  $p$  represent electron mass, speed of light, Pauli matrices, and electron momentum, respectively. Another contribution to the SOC is the intra-molecular SOC (19, 20, 42, 43), which takes the form  $\hbar/(4m_e^2c^2)[\nabla V \cdot (\sigma \times p)]$ , where  $V$  is the electrostatic potential of helically stacked monomers. These SOC mechanisms induce spin-dependent electron deflection, generating ISHE and ICISS.

Figures 1B and 1C schematically depict electron transport behaviors of ISHE and ICISS, respectively. A  $+z$ -polarized spin current is injected from the spin injector layer into the chiral molecular layer, and the molecular chiral axis  $\Omega_{R/S}$  is oriented along the  $z$ -axis. In ISHE (Fig. 1B), electrons with  $+z$ -aligned spins are deflected toward the  $+y$  surface due to SOC, while those with the opposite spin are diverted through the  $-y$  surface back into the spin injector layer, as illustrated by the red curved arrows. This mechanism establishes a net charge current in  $y$  direction, creating transverse charge accumulation that manifests as a non-zero ISHE signal  $V_y$ . In ICISS (Fig. 1C), the transmission probabilities of electrons from the spin injector layer to the  $+z$ -oriented and  $-z$ -oriented surfaces are different because of the chiral structure and SOC (23, 42, 44), and the transmission difference depends on the spin polarization direction  $\sigma_s$  and the molecular chiral axis  $\Omega_{R/S}$  (19, 20, 23, 42). As illustrated in Fig. 1C, electrons with  $+z$ -aligned spins exhibit preferential propagation toward the  $+z$ -oriented surface while being suppressed at the  $-z$ -oriented surface (23, 42). This leads to a transverse charge transfer along the chiral axis  $\Omega_{R/S}$ , giving rise to ICISS. In real experimental systems, disorder inevitably arises owing to misalignment, defects, or impurities

(45). In the following, we also demonstrate through numerical calculations that these effects persist even in the presence of strong disorder.

**Transport behavior of ISHE and ICIS.** Next, we sequentially investigate the transport behavior of each experimental configuration using the non-equilibrium Green's function method (36–38) (SI Appendix). In all configurations, the molecular chiral axis  $\Omega_{R/S}$  is aligned along the  $z$  direction, and the spin current  $J_s$  flows in the  $-x$  direction. In the first configuration shown in the inset of Fig. 2A, the spin polarization direction  $\sigma_s$  is along the  $+z$  direction, while the voltage  $V_y = V_{+y} - V_{-y}$  is measured along the  $y$  direction, where  $V_{+y}$  and  $V_{-y}$  are the voltages of the  $+y/-y$  surfaces, respectively. Since the voltage measurement direction is perpendicular to  $\sigma_s$ , this corresponds to the ISHE voltage (30). The green line and orange dashed line in Fig. 2A show the  $V_y$  signal versus the system's Fermi energy  $E$  for right-handed and left-handed molecules, respectively. Several important features can be identified: (i) A non-zero ISHE signal  $V_y$  appears when  $E$  lies within the system's energy band. The absolute value of  $V_y$  increases near the band edges, while  $V_y = 0$  outside the band range. (ii) The  $V_y$  curve also exhibits oscillating behavior, with the oscillations intensifying near the band edges. These oscillations are caused by quantum interference, consistent with our previous studies (42). (iii)  $V_y$  is positive for  $E < 0$  and negative for  $E > 0$ . (iv) The  $V_y - E$  curve possesses central symmetry with respect to the point (0,0), i.e.,  $V_y(-E) = -V_y(E)$ , which originates from electron-hole symmetry (42) (SI Appendix). (v) Crucially, when the molecular chirality is reversed (changing from the right-handed green line to the left-handed orange dashed line, with the structure parameters change as  $\theta_{mol} \rightarrow \pi - \theta_{mol}$ ,  $\Delta\varphi \rightarrow -\Delta\varphi$ , SI Appendix), the two curves completely coincide. This demonstrates that the ISHE signal is entirely independent of molecular chirality, in agreement with experimental results (30). To investigate the effect of disorder on this ISHE, we calculate and statistically analyze the ISHE  $V_y$  signal at  $E = -4t_1$  ( $t_1$  is the intra-chain hopping integral, SI Appendix) for 1000 disorder configurations in SI Appendix, Fig. S1A. Results show that even under strong disorder ( $W = t_1$ ), the  $V_y$  signal changes very little, exhibiting only slight broadening. This indicates that the ISHE in this system is highly robust.

The inset of Fig. 2B shows the second experimental configuration, where the spin polarization direction  $\sigma_s$  of the spin current is along the  $+y$  direction, and the voltage  $V_z = V_{+z} - V_{-z}$  is measured along the  $z$  direction, where  $V_{+z}$  and  $V_{-z}$  are the voltages of the  $+z/-z$  surfaces, respectively. Since the measurement direction remains perpendicular to the spin polarization direction  $\sigma_s$ , this also corresponds to the ISHE voltage (30). The green line and orange dashed line in Fig. 2B show the  $V_z$  signal versus  $E$  for right-handed and left-handed molecules, respectively. It reveals that the  $z$  direction also produces an ISHE signal similar to that in the  $y$  direction, except for the difference in feature (iii): Here,  $V_z < 0$  for  $E < 0$  and  $V_z > 0$  for  $E > 0$ . This phenomenon is fully

understandable: In the ISHE,  $J_c \propto J_s \times \sigma_s$ ; therefore, when  $E < 0$ , electrons with spin polarized along  $+y$  are deflected towards the  $-z$  direction, leading to a charge current along  $-z$ . Since this opposes the defined  $V_z$  measurement direction ( $+z$ ), the measured voltage is negative. It is shown in Figs. 2A and 2B that the ISHE signal appears as long as the measurement direction is perpendicular to both  $\sigma_s$  and the flow direction of the spin current (i.e.  $J_c \propto J_s \times \sigma_s$ ), regardless of whether  $\sigma_s$  is parallel (Fig. 2A) or perpendicular (Fig. 2B) to  $\Omega_{R/S}$ . We also studied the  $z$  direction ISHE under 1000 disorder configurations in SI Appendix, Fig. S1B, confirming its strong robustness against disorder.

Next, we investigate the ICISS according to the experimental configurations (30). The inset in Fig. 2C shows the experimental setup for measuring the  $z$  direction ICISS. There, both the spin polarization direction  $\sigma_s$  and the voltage measurement direction are along the  $+z$  direction (30), parallel to the molecular chiral axis  $\Omega_{R/S}$  (i.e., the  $z$  direction). The green and orange lines in Fig. 2C show the  $V_z$  signal versus the system's Fermi energy  $E$  for right-handed and left-handed molecules, respectively. We observe that a non-zero ICISS signal indeed shows up, exhibiting both similarities to and distinctions from the ISHE. First, similar to the ISHE, the non-zero ICISS signal only exists within the band, reaches its maximum near the band edges, and shows oscillatory behavior. Furthermore, the ICISS curve also possesses central symmetry with respect to the point (0,0), guaranteed by the electron-hole symmetry of the Hamiltonian. However, ICISS and ISHE exhibit significant distinctions. In ICISS, the electron deflection occurs along the direction of  $\Omega_{R/S}$ , thus the resultant voltage is in the  $z$  direction, as illustrated in Fig. 1C. Importantly, when the molecular chirality is reversed (changing from the right-handed green line to the left-handed orange line, with structure parameters change as  $\theta_{mol} \rightarrow \pi - \theta_{mol}$ ,  $\Delta\varphi \rightarrow -\Delta\varphi$ ), the ICISS signal  $V_z$  also reverses sign to  $-V_z$ . This demonstrates that ICISS is highly dependent on molecular chirality, in agreement with experimental results (30). In SI Appendix, Fig. S1C, we examine the effect of disorder on ICISS, and a strong robustness against disorder is observed.

To explore the relationship between ICISS and the molecular chiral structure, we study the voltage signal measured along the  $y$  direction with  $\sigma_s$  along the  $+y$  direction, as shown in the inset of Fig. 2D. Here, the voltage measurement direction is still parallel to  $\sigma_s$  (both are in the  $+y$  direction), so the measured signal is the ICISS signal (30). However, unlike Fig. 2C, both the voltage measurement direction and  $\sigma_s$  are perpendicular to  $\Omega_{R/S}$ . Fig. 2D reveals that the voltage  $V_y$  in the  $y$  direction is small, demonstrating that ICISS, like CISS, predominantly occurs along  $\Omega_{R/S}$ . While the ICISS signal is small, it is non-zero and also reverses its sign when the molecular chirality is reversed. Surprisingly, we note that a similar small chirality-dependent signal was indeed observed experimentally (30), indicating perfect agreement between our model and the

experimental observations. SI Appendix, Fig. S1D shows the effect of disorder on the  $y$  direction ICISS signal, confirming that it remains small and is largely unaffected by disorder.

**Spin-polarization-angle dependence of ISHE and ICISS.** We further investigate the dependence of ISHE and ICISS on the spin polarization direction  $\sigma_s$  of the injected spin current, following the experimental configurations (30). The molecular chiral axis  $\Omega_{R/S}$  is always aligned along the  $z$  direction. We first investigate the case where  $\sigma_s$  lies within the  $xz$  plane, following the experimental configuration, shown in the inset of Fig. 3A. Here, the angle between  $\sigma_s$  and the positive  $z$ -axis is denoted as  $\theta_1$ . Figure 3A shows the variation of the  $y$  direction voltage  $V_y$  with  $\theta_1$  (ranging from 0 to  $2\pi$ ) for molecules of different chirality (right-handed: green line; left-handed: orange dashed line) at  $E = -4t_1$ . Since the in-plane ( $yz$  plane) component of the spin lies along the  $z$  direction, and the voltage is measured along the  $y$  direction, only the ISHE is present here. Because the component of  $\sigma_s$  within the  $yz$  plane varies as  $\cos \theta_1$ , the voltage in the  $y$  direction follows  $V_y(\theta_1) = V_{y,ISHE} \cos \theta_1$ , where  $V_{y,ISHE} = V_y(0)$ . At  $\theta_1 = \pi/2, 3\pi/2$ , the in-plane spin component is zero, resulting in no spin deflection and thus  $V_y = 0$ . At  $\theta_1 = \pi$ , the spin polarization is along the  $-z$  direction; the electron deflection direction reverses, leading to  $V_y(\pi) = -V_y(0)$ , obeying  $J_c \propto J_s \times \sigma_s$ . Crucially, the  $V_y$  curves for different chiral molecules completely coincide, demonstrating the independence of ISHE from molecular chirality (30).

Figure 3B shows the variation of the  $z$  direction voltage  $V_z$  with  $\theta_1$  for molecules of different chirality at  $E = -4t_1$ , with  $\theta_1$  defined identically to Fig. 3A. Since both the measurement direction and the projection direction of the spin within the  $yz$  plane are along  $z$ , only ICISS is present here. As  $\theta_1$  increases, the projection component of the spin polarization along  $\Omega_{R/S}$  also varies as  $\cos \theta_1$ . Therefore, the  $z$  direction voltage follows  $V_z(\theta_1) = V_{z,ICISS} \cos \theta_1$ , where  $V_{z,ICISS} = V_z(0)$ . When  $\sigma_s$  is perpendicular to  $\Omega_{R/S}$  ( $\theta_1 = \pi/2, 3\pi/2$ ), the spin selectivity effect does not occur, resulting in  $V_z(\theta_1) = 0$ . When the spin polarization direction is anti-parallel to the chiral axis ( $\theta_1 = \pi$ ), the opposite spin selectivity effect occurs. Significantly, the  $V_z$  curves for molecules of opposite chirality have exact opposite signs. This occurs because ICISS is determined by molecular chirality.

All preceding results (Figs. 2, 3A-3B) derive from theoretical calculations replicating experimental measurement configurations, showing great agreement with experiment (30). We now extend our investigation to the experimentally uncharted regime where  $\sigma_s$  rotates within the  $yz$ -plane (the film plane). In Figs. 3C and 3D, the angle between  $\sigma_s$  and the positive  $z$ -axis is denoted as  $\theta_2$ , shown in the inset of Fig. 3C. Figure 3C shows the variation of the  $y$  direction voltage  $V_y$  with  $\theta_2$  at  $E = -4t_1$ . As established by Figs. 2A and 2D, the molecular layer can generate a significant ISHE and a weak ICISS in the  $y$  direction. Therefore, the primary

characteristic of  $V_y$  is determined by the projection magnitude of  $\sigma_s$  within the  $xz$  plane, similar to Fig. 3A. However, due to the presence of a small ICISS in the  $y$  direction, the superposition of these two effects causes a small phase shift in the curve. For the right-handed molecules (green line in Fig. 3C), when  $\sigma_s$  is along  $+z$  ( $\theta_2 = 0$ ) and along  $+y$  ( $\theta_2 = \pi/2$ ), the voltage in the  $y$  direction is entirely due to ISHE and ICISS, respectively, denoted as  $V_{y,ISHE}$  and  $V_{y,ICISS}$ . When  $\theta_2$  is at other values, the contributions to the  $y$  direction voltage from ISHE and ICISS are given by  $V_{y,ISHE} \cos \theta_2$  and  $V_{y,ICISS} \sin \theta_2$ , respectively. The total voltage  $V_y(\theta_2)$  is then the sum of these two contributions: 
$$V_y(\theta_2) = V_{y,ISHE} \cos \theta_2 + V_{y,ICISS} \sin \theta_2 = \sqrt{V_{y,ISHE}^2 + V_{y,ICISS}^2} \cos(\theta_2 - \varphi_y),$$
 where  $\varphi_y = \arctan(V_{y,ICISS}/V_{y,ISHE})$  is very small, because  $V_{y,ICISS}$  is very small (see Fig. 2D). From Fig. 3C, we indeed observe that  $V_y$  is not strictly zero at  $\theta_2 = \pi/2$  and  $\theta_2 = 3\pi/2$ , equating to  $V_{y,ICISS}$  and  $-V_{y,ICISS}$ , respectively. At  $\theta_2 = \pi$ , the electron deflection direction reverses compared to  $\theta_2 = 0$ , leading to  $V_y(\pi) = -V_y(0)$ . When the molecular chirality is reversed, for the left-handed molecules (orange line in Fig. 3C),  $V_y(\theta_2) = \sqrt{V_{y,ISHE}^2 + V_{y,ICISS}^2} \cos(\theta_2 + \varphi_y)$ . The change of sign ( $-\varphi_y \rightarrow \varphi_y$ ) originates from the change in chirality, resulting in a slight separation between the curves for left- and right-handed molecules, unlike the complete coincidence in Fig. 3A.

Figure 3D shows the variation of the  $z$  direction voltage  $V_z$  with  $\theta_2$  at  $E = -4t_1$ . As shown in Figs. 2B and 2C, the molecular layer can simultaneously generate both ISHE and ICISS in  $z$  direction, leading to richer electron transport behavior. When  $\sigma_s$  is along  $+z$  ( $\theta_2 = 0$ ) and along  $+y$  ( $\theta_2 = \pi/2$ ), the voltage in the  $z$  direction is entirely due to ICISS and ISHE, respectively, denoted as  $V_{z,ICISS}$  and  $V_{z,ISHE}$ . Following analysis similar to Fig. 3C, we conclude that  $V_z(\theta_2) = \sqrt{V_{z,ICISS}^2 + V_{z,ISHE}^2} \cos(\theta_2 \mp \varphi_z)$ , where  $\varphi_z = \arctan(V_{z,ISHE}/V_{z,ICISS})$  is the phase shift induced by the cooperative action of ISHE and ICISS, and the sign ( $\mp$ ) depends on molecular chirality. Taking the green line (right-handed) in Fig. 3D as an example, we illustrate how ISHE and ICISS compete and synergize in spin-to-charge conversion: As  $\theta_2$  increases from 0 to  $\pi/2$ , the projections of the spin polarization in both the  $y$  and  $z$  directions are positive. According to Figs. 2B and 2C, ISHE induces a charge current towards  $-z$ , while ICISS induces an opposing charge current towards  $+z$ . This competition causes the  $V_z$  curve to decrease rapidly, reaching  $V_z = 0$  at  $\theta_2 \approx 0.4\pi$ , smaller than  $\theta_2 = \pi/2$  in Fig. 3B. At  $\theta_2 = \pi/2$ ,  $\sigma_s$  is entirely along the  $+y$  direction, meaning only ISHE contributes; since ISHE is chirality-independent (Fig. 2B), the green line intersects the orange line (opposite chirality) at this point. As  $\theta_2$  increases further beyond  $\pi/2$ , both ISHE and ICISS induce a charge current towards  $-z$ . This synergy causes the absolute value  $|V_z|$  to reach a maximum

at  $\theta_2 \approx 0.9\pi$ . When  $\theta_2$  increases from  $0.9\pi$  to  $\pi$ ,  $|V_z|$  slightly decreases due to the reduced contribution from ISHE. For  $\theta_2$  ranging from  $\pi$  to  $2\pi$ , the effects first compete and then synergize again; at  $\theta_2 = 3\pi/2$ , only the chirality-independent ISHE contributes, so two lines intersect once more. The results in Fig. 3 collectively demonstrate that within the chiral molecular layer, ISHE and ICISS can be studied both individually (Figs. 3A, 3B) and simultaneously (Figs. 3C, 3D), where ICISS can be independently controlled via molecular chirality. These findings indicate that chiral molecular layers provide a highly promising platform for studying and manipulating spin conversion mechanisms in spintronics.

**Size dependence of ISHE and ICISS.** Finally, we investigate the size dependence of ISHE and ICISS in the molecular layer with respect to the size parameters  $L_x$ ,  $L_y$ , and  $L_z$ . In Fig. 4,  $\sigma_s$  is fixed along the  $+z$  direction, the molecule is right-handed, with chiral axis along the  $z$  direction, and the Fermi energy is fixed at  $E = -4t_1$ , such that  $V_y$  represents the ISHE signal (same as Fig. 2A) and  $V_z$  represents the ICISS signal (same as Fig. 2C). Figure 4A shows the variation of  $V_y$  and  $V_z$  with thickness  $L_x$  while fixing  $L_y = L_z = 25$ . The results reveal that both ISHE and ICISS signals initially increase with  $L_x$ , reach a maximum at  $L_x = 4$ , and decrease inversely with further increases in  $L_x$ . This behavior arises because electron spins undergo precession and relaxation due to SOC, leading to a finite spin diffusion length  $\lambda_s$ . For  $L_x < \lambda_s$ , spin accumulation within the system generates a backflow spin current opposing the injected spin current, resulting in a smaller net injected spin current under a fixed spin bias in very thin samples (4). As  $L_x$  increases, the backflow diminishes and the injected spin current increases. Since both ISHE and ICISS convert spin current into transverse charge current, we have the transverse charge current  $I_y \propto |J_s|$  and  $I_z \propto |J_s|$ . The sample resistances in the  $y$  and  $z$  directions are proportional to  $R_y \propto L_y/(L_x L_z)$  and  $R_z \propto L_z/(L_x L_y)$ , respectively. Consequently,  $V_y = I_y R_y \propto |J_s|/L_x$  and  $V_z = I_z R_z \propto |J_s|/L_x$ . When  $L_x < \lambda_s$ , both  $V_y$  and  $V_z$  increase, indicating  $|J_s|$  increases faster than  $L_x$ . When  $L_x > \lambda_s$ , the spin current magnitude  $|J_s|$  saturates, causing both  $V_y$  and  $V_z$  to decrease inversely with  $L_x$  for larger thicknesses, fully consistent with established ISHE experimental results (6). Our findings thus predict that ICISS exhibits the same thickness dependence as ISHE.

Figure 4B shows the variation of  $V_y$  and  $V_z$  with molecular layer width  $L_y$  while fixing  $L_x = 4$  and  $L_z = 25$ . The results indicate that the ISHE signal  $V_y$  gradually increases with  $L_y$ , albeit with a decreasing slope. Strikingly, the ICISS signal  $V_z$  remains almost constant regardless of  $L_y$ . The underlying physical mechanism is as follows: Under fixed spin bias, the magnitude of the injected spin current  $|J_s|$  is proportional to the area of the  $yz$  interface, i.e.,  $|J_s| \propto L_y L_z$ . Based on the derived relations  $V_y = I_y R_y \propto L_y^2/L_x$  and  $V_z = I_z R_z \propto L_z^2/L_x$ ,  $V_y$  increases with  $L_y$  while  $V_z$  is independent of  $L_y$ . Spin relaxation along the  $y$  direction causes the growth rate of  $V_y$  to slow down for larger  $L_y$ .

The increase of  $V_y$  with  $L_y$  matches ISHE experimental observations (6), and our results therefore predict that ICISS is independent of the molecular layer width.

Figure 4C shows the variation of  $V_y$  and  $V_z$  with molecular length  $L_z$  while fixing  $L_x = 4$  and  $L_y = 25$ . The figure reveals that ISHE signal remains almost constant for larger  $L_z$ , while ICISS signal  $V_z$  increases with  $L_z$  before saturating, exhibiting the opposite trend to Fig. 4B. Analysis similar to that for Fig. 4B readily explains these results. The observed length dependence of ISHE well matches experimental findings (6). Meanwhile, the length dependence of ICISS closely resembles the variation of spin polarization with molecular length in CISS (20, 26, 46). Our theory therefore predicts that ICISS exhibits the same dependence on molecular length as observed in CISS.

## Discussion

In conclusion, we propose a theoretical model based on the experimental configuration (30), and obtain ISHE and ICISS consistent with experimental results. We demonstrate that the experimentally observations originate from the SOC arises from the heterojunction and the helically stacked monomers. Both effects persist even in the strong disorder. The charge current generated by ISHE satisfies  $J_c \propto J_s \times \sigma_s$ , and the charge current generated by ICISS satisfies  $J_c \propto \Omega_{R/S}$ . Furthermore, we predict that mutual competition and synergy emerge between ISHE and ICISS upon variation of  $\sigma_s$  within the chiral molecular plane. This unexplored, yet fascinating, phenomenon serves as a crucial guide for subsequent experimental investigations. Finally, ISHE and ICISS show distinct dependencies on the system size. We provide a comprehensive explanation of the ICISS effect and are expected to advance the development of organic-based spintronics.

## Materials and Methods

The Hamiltonian model describing the chiral molecular layer (19, 20, 23, 43), the spin injector layer, and electrodes along the  $y$  and  $z$  directions based on the experimental configuration (30, 47, 48) can be found in “Model Hamiltonian” section in SI Appendix. The voltage along the  $y$  and  $z$  directions are calculated using the standard non-equilibrium Green’s function method (38) (details can be found in “Transport formulation” section in SI Appendix). Model parameters of the Hamiltonian model can be found in “Model parameters” section in SI Appendix.

**Data, Materials, and Software Availability.** All study data are included in the article and/or SI Appendix.

**Acknowledgments.** This work was financially supported by the National Key R and D Program of China (Grant No. 2024YFA1409002), the National Natural Science Foundation of China (Grant No. 12374034 and No. 12274466), the Innovation Program for Quantum Science and Technology (2021ZD0302403), and the Hunan Provincial Science Fund for Distinguished Young Scholars (2023JJ10058). We also acknowledge the High-performance Computing Platform of Peking University for providing computational resources.

## References

1. S. A. Wolf, *et al.*, Spintronics: A Spin-Based Electronics Vision for the Future. *Science* **294**, 1488–1495 (2001).
2. A. Hirohata, *et al.*, Review on spintronics: Principles and device applications. *Journal of Magnetism and Magnetic Materials* **509**, 166711 (2020).
3. J. E. Hirsch, Spin Hall Effect. *Phys. Rev. Lett.* **83**, 1834–1837 (1999).
4. J. Sinova, S. O. Valenzuela, J. Wunderlich, C. H. Back, T. Jungwirth, Spin Hall effects. *Rev. Mod. Phys.* **87**, 1213–1260 (2015).
5. E. Saitoh, M. Ueda, H. Miyajima, G. Tatara, Conversion of spin current into charge current at room temperature: Inverse spin-Hall effect. *Applied Physics Letters* **88**, 182509 (2006).
6. K. Ando, *et al.*, Inverse spin-Hall effect induced by spin pumping in metallic system. *Journal of Applied Physics* **109**, 103913 (2011).
7. S. Manipatruni, *et al.*, Scalable energy-efficient magnetoelectric spin–orbit logic. *Nature* **565**, 35–42 (2019).
8. K. Ray, S. P. Ananthavel, D. H. Waldeck, R. Naaman, Asymmetric Scattering of Polarized Electrons by Organized Organic Films of Chiral Molecules. *Science* **283**, 814–816 (1999).
9. B. Göhler, *et al.*, Spin Selectivity in Electron Transmission Through Self-Assembled Monolayers of Double-Stranded DNA. *Science* **331**, 894–897 (2011).
10. R. Nakajima, *et al.*, Giant spin polarization and a pair of antiparallel spins in a chiral superconductor. *Nature* **613**, 479–484 (2023).

11. B. P. Bloom, Y. Paltiel, R. Naaman, D. H. Waldeck, Chiral Induced Spin Selectivity. *Chem. Rev.* **124**, 1950–1991 (2024).
12. R. Naaman, Y. Paltiel, D. H. Waldeck, Chiral molecules and the electron spin. *Nat Rev Chem* **3**, 250–260 (2019).
13. Z. Xie, *et al.*, Spin Specific Electron Conduction through DNA Oligomers. *Nano Lett.* **11**, 4652–4655 (2011).
14. T. K. Das, N. Preeyanka, S. Mishra, Y. Sang, C. Fontanesi, Spin-selective anisotropic magnetoresistance driven by chirality in DNA. *Adv Funct Materials* 2425377 (2025).
15. S. Mishra, S. Pirbadian, A. K. Mondal, M. Y. El-Naggar, R. Naaman, Spin-Dependent Electron Transport through Bacterial Cell Surface Multiheme Electron Conduits. *J. Am. Chem. Soc.* **141**, 19198–19202 (2019).
16. Y. Xu, W. Mi, Chiral-induced spin selectivity in biomolecules, hybrid organic–inorganic perovskites and inorganic materials: a comprehensive review on recent progress. *Mater. Horiz.* **10**, 1924–1955 (2023).
17. Q. Qian, *et al.*, Chiral molecular intercalation superlattices. *Nature* **606**, 902–908 (2022).
18. C.-H. Ko, *et al.*, Twisted molecular wires polarize spin currents at room temperature. *Proc. Natl. Acad. Sci. U.S.A.* **119**, e2116180119 (2022).
19. A.-M. Guo, Q.-F. Sun, Spin-Selective Transport of Electrons in DNA Double Helix. *Phys. Rev. Lett.* **108**, 218102 (2012).
20. A.-M. Guo, Q.-F. Sun, Spin-dependent electron transport in protein-like single-helical molecules. *Proc. Natl. Acad. Sci. U.S.A.* **111**, 11658–11662 (2014).
21. S. Alwan, Y. Dubi, Spinterface Origin for the Chirality-Induced Spin-Selectivity Effect. *J. Am. Chem. Soc.* **143**, 14235–14241 (2021).
22. T. K. Das, F. Tassinari, R. Naaman, J. Fransson, Temperature-Dependent Chiral-Induced Spin Selectivity Effect: Experiments and Theory. *J. Phys. Chem. C* **126**, 3257–3264 (2022).
23. T.-Y. Zhang, Y. Mao, A.-M. Guo, Q.-F. Sun, Dynamical theory of chiral-induced spin selectivity in electron donor–chiral molecule–acceptor systems. *Phys. Rev. B* **111**, 205417 (2025).
24. Y. Zhao, K. Zhang, J. Xiao, K. Sun, B. Yan, Magnetochiral charge pumping due to charge trapping and skin effect in chirality-induced spin selectivity. *Nat Commun* **16**, 37 (2025).
25. P.-Y. Liu, T.-Y. Zhang, Q.-F. Sun, Dynamical Simulation of Chiral-Induced Spin-Polarization and Magnetization. *J. Phys. Chem. Lett.* 6500–6506 (2025).

26. R. Gutierrez, E. Díaz, R. Naaman, G. Cuniberti, Spin-selective transport through helical molecular systems. *Phys. Rev. B* **85**, 081404 (2012).
27. O. Ben Dor, *et al.*, Magnetization switching in ferromagnets by adsorbed chiral molecules without current or external magnetic field. *Nat Commun* **8**, 14567 (2017).
28. H. Aizawa, *et al.*, Enantioselectivity of discretized helical supramolecule consisting of achiral cobalt phthalocyanines via chiral-induced spin selectivity effect. *Nat Commun* **14**, 4530 (2023).
29. Y. Adhikari, *et al.*, Interplay of structural chirality, electron spin and topological orbital in chiral molecular spin valves. *Nat Commun* **14**, 5163 (2023).
30. R. Sun, *et al.*, Inverse chirality-induced spin selectivity effect in chiral assemblies of  $\pi$ -conjugated polymers. *Nat. Mater.* **23**, 782–789 (2024).
31. K. S. Park, *et al.*, Chiral emergence in multistep hierarchical assembly of achiral conjugated polymers. *Nat Commun* **13**, 2738 (2022).
32. A. Moharana, *et al.*, Chiral-induced unidirectional spin-to-charge conversion. *Sci. Adv.* **11**, eado4285 (2025).
33. A. Brataas, Y. Tserkovnyak, G. E. W. Bauer, B. I. Halperin, Spin battery operated by ferromagnetic resonance. *Phys. Rev. B* **66**, 060404 (2002).
34. D.-K. Wang, Q.-F. Sun, H. Guo, Spin-battery and spin-current transport through a quantum dot. *Phys. Rev. B* **69**, 205312 (2004).
35. Q.-F. Sun, X. C. Xie, Definition of the spin current: The angular spin current and its physical consequences. *Phys. Rev. B* **72**, 245305 (2005).
36. Y. Xing, Q.-F. Sun, J. Wang, Symmetry and transport property of spin current induced spin-Hall effect. *Phys. Rev. B* **75**, 075324 (2007).
37. D. H. Lee, J. D. Joannopoulos, Simple scheme for surface-band calculations. I. *Phys. Rev. B* **23**, 4988–4996 (1981).
38. S. Datta, *Electronic Transport in Mesoscopic Systems*, 1st Ed. (Cambridge University Press, 1995).
39. V. M. Edelstein, Spin polarization of conduction electrons induced by electric current in two-dimensional asymmetric electron systems. *Solid State Communications* **73**, 233–235 (1990).
40. Y. A. Bychkov, E. I. Rashba, Oscillatory effects and the magnetic susceptibility of carriers in inversion layers. *J. Phys. C: Solid State Phys.* **17**, 6039–6045 (1984).

41. Y. Xing, Q.-F. Sun, L. Tang, J. Hu, Accumulation of opposite spins on the transverse edges of a two-dimensional electron gas in a longitudinal electric field. *Phys. Rev. B* **74**, 155313 (2006).
42. T.-R. Pan, A.-M. Guo, Q.-F. Sun, Spin-polarized electron transport through helicene molecular junctions. *Phys. Rev. B* **94**, 235448 (2016).
43. C. Wang, *et al.*, Transverse Spin Selectivity in Helical Nanofibers Prepared without Any Chiral Molecule. *Phys. Rev. Lett.* **133**, 108001 (2024).
44. Q.-F. Sun, J. Wang, H. Guo, Quantum transport theory for nanostructures with Rashba spin-orbital interaction. *Phys. Rev. B* **71**, 165310 (2005).
45. W. Long, Q.-F. Sun, J. Wang, Disorder-Induced Enhancement of Transport through Graphene p – n Junctions. *Phys. Rev. Lett.* **101**, 166806 (2008).
46. S. Mishra, *et al.*, Length-Dependent Electron Spin Polarization in Oligopeptides and DNA. *J. Phys. Chem. C* **124**, 10776–10782 (2020).
47. H. Song, H. Lee, T. Lee, Intermolecular Chain-to-Chain Tunneling in Metal–Alkanethiol–Metal Junctions. *J. Am. Chem. Soc.* **129**, 3806–3807 (2007).
48. T. Frederiksen, *et al.*, Exploring the Tilt-Angle Dependence of Electron Tunneling across Molecular Junctions of Self-Assembled Alkanethiols. *ACS Nano* **3**, 2073–2080 (2009).

## Figures and Tables

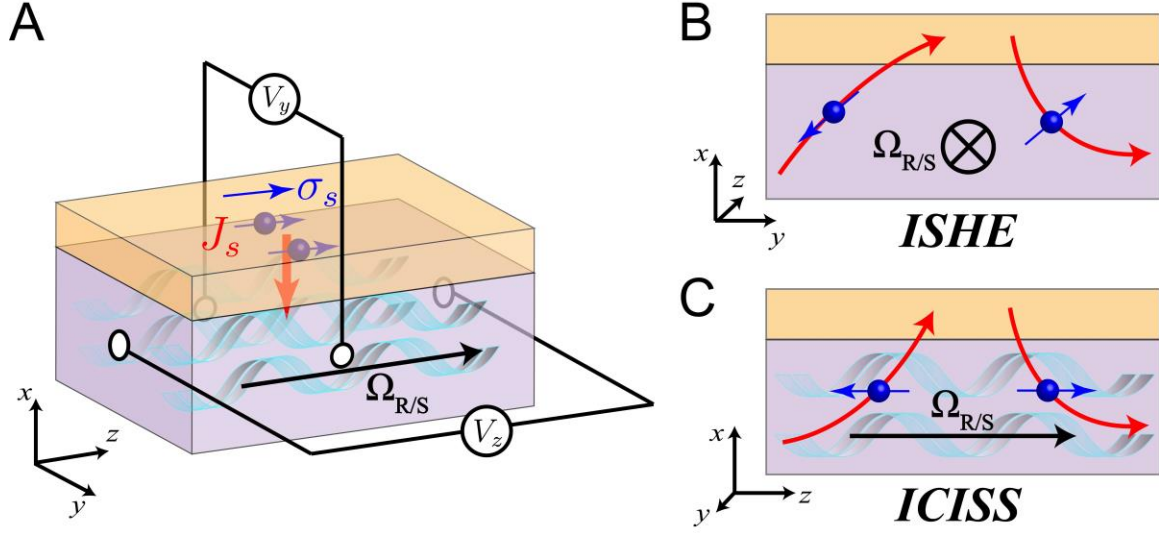


**Fig. 1.** Schematic diagram of the model, ISHE and ICISS. (A) Schematic diagram of the experimental measurement configuration. The orange and purple boxes represent the spin injector layer and the chiral molecular layer, respectively. The spin injector layer injects a spin current  $J_s$  toward the  $-x$  direction into the chiral molecular layer. The spin polarization direction  $\sigma_s$  and the spin current flow direction  $J_s$  are indicated by the blue arrow and red arrow, respectively. The chiral axis  $\Omega_{R/S}$  of the chiral molecular layer is parallel to the  $+z$  direction. Voltage probes  $V_y$  and  $V_z$  are connected along the  $y$  and  $z$  directions of the chiral molecular layer. (B) Schematic diagram of the ISHE. Within the  $xy$ -plane perpendicular to  $\Omega_{R/S}$ , electrons with spin parallel to  $+z$  and electrons with spin parallel to  $-z$  are deflected in opposite directions, leading to a charge current along the  $y$  direction. (C) Schematic diagram of the ICISS. Within the  $xz$ -plane parallel to  $\Omega_{R/S}$ , electrons with spin parallel to  $+z$  and electrons with spin parallel to  $-z$  are deflected in opposite directions, leading to a charge current along the  $z$  direction.

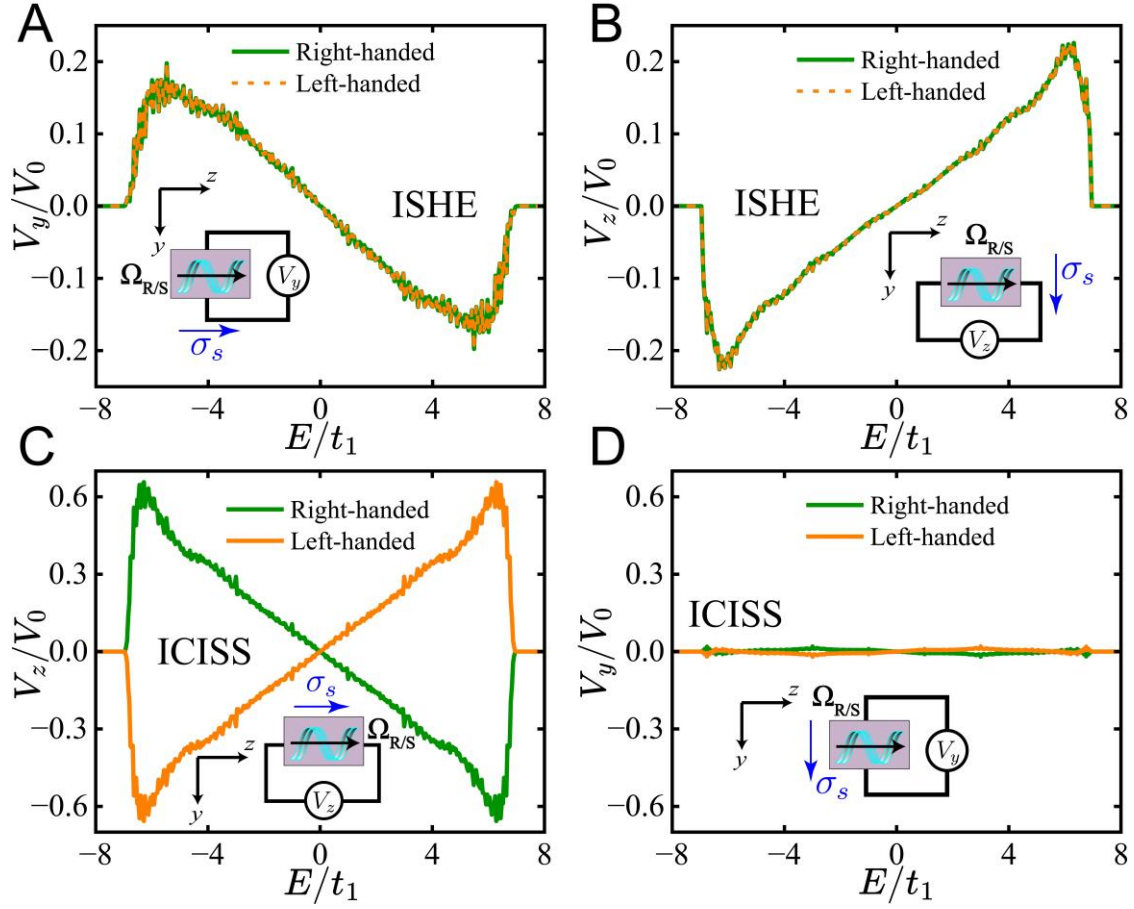


**Fig. 2.** Transport properties of ISHE and ICISS. (A-B) Energy  $E$  dependence of the ISHE voltage in the right-handed (green line) and left-handed (orange dashed line) chiral molecular layer. (A) Voltage  $V_y$  is measured along the  $+y$  direction, and the spin polarization direction is along the  $+z$  direction. (B) Voltage  $V_z$  is measured along the  $+z$  direction, and the spin polarization direction is along the  $+y$  direction. (C-D) Energy  $E$  dependence of the ICISS voltage in the chiral molecular layer. (C) Both the spin polarization direction and the voltage  $V_z$  measurement direction are along the  $+z$  direction. (D) Both the spin polarization direction and the voltage  $V_y$  measurement direction are along the  $+y$  direction. The inset of each panel illustrates the corresponding measurement configuration, where the spin current polarization direction  $\sigma_s$  is marked by blue arrow, molecular chiral axis  $\Omega_{R/S}$  is along the  $+z$  direction. The Fermi energy is  $E = -4t_1$ , and other parameters used here are provided in SI Appendix.

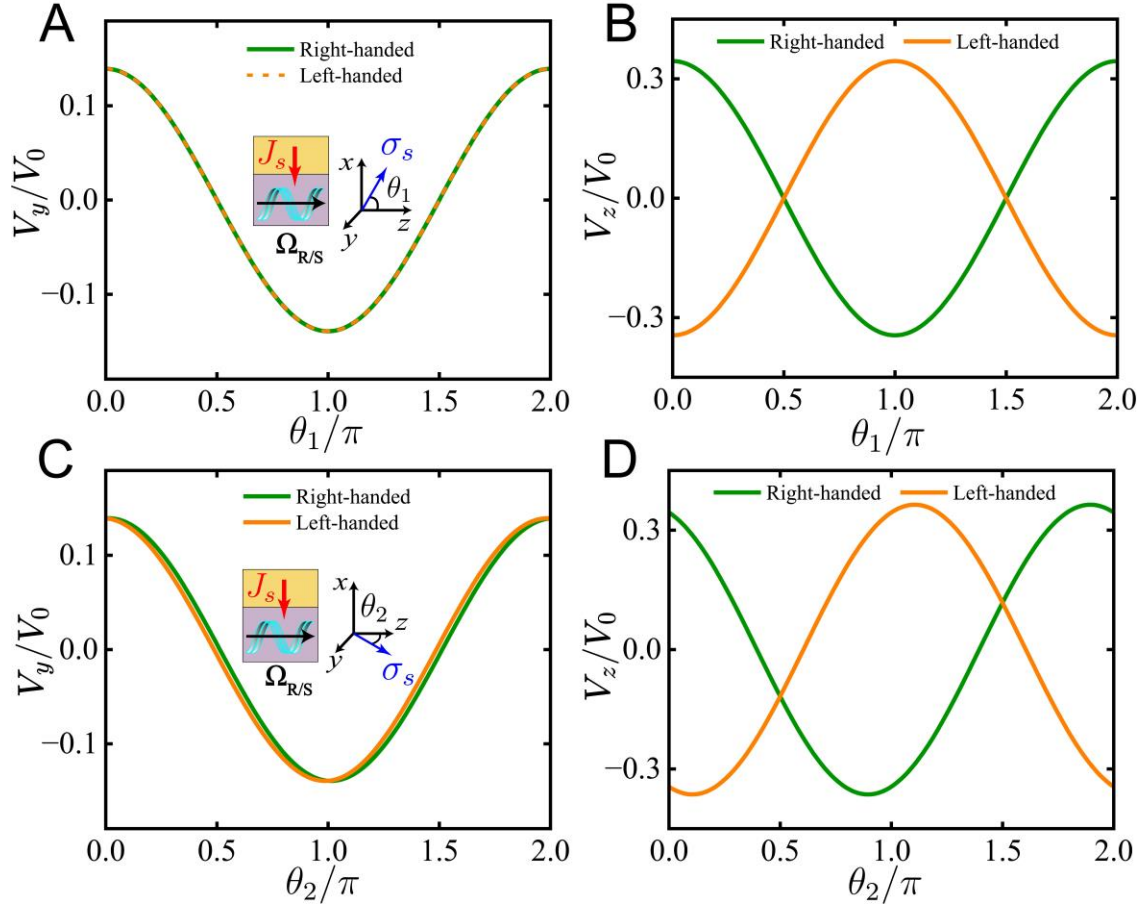


**Fig. 3.** Spin-polarization-angle-dependence of ISHE and ICIS. (A-B) Voltage variation along the  $y$  (A) and  $z$  directions (B) as the spin current polarization direction  $\sigma_s$  rotates within the  $xz$ -plane (angle  $\theta_1$  relative to the  $z$ -axis, shown in the inset of A).  $J_s$  is the direction of spin current flow. (C-D) Voltage variation along the  $y$  (C) and  $z$  directions (D) as the spin current polarization direction  $\sigma_s$  rotates within the  $yz$ -plane (angle  $\theta_2$  relative to the  $z$ -axis, shown in the inset of C). Here the chiral axis  $\Omega_{R/S}$  is along the  $z$  direction, Fermi energy is  $E = -4t_1$ , and other parameters used here are provided in SI Appendix.

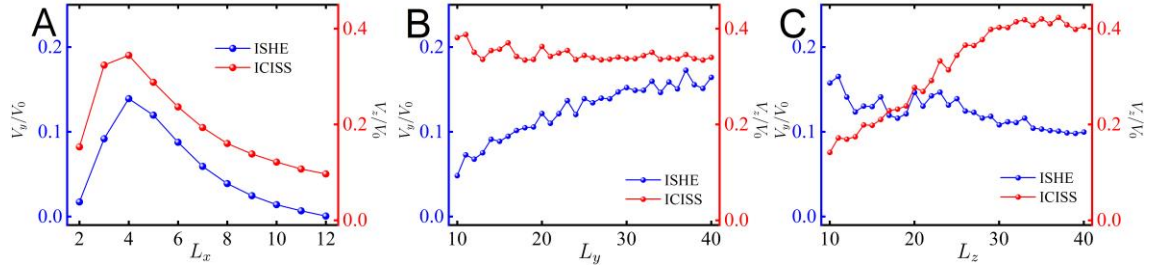


**Fig. 4.** Size dependence of ISHE and ICISS. (A-C) Dependence of ISHE and ICISS,  $V_y$  and  $V_z$ , on molecular layer thickness  $L_x$  in (A), on molecular layer width  $L_y$  in (B), and on molecular length  $L_z$  in (C). The molecular dimensions are fixed at  $L_x = 4$  and  $L_y = L_z = 25$ , unless they serve as the horizontal axis (variable). The Fermi energy is  $E = -4t_1$ , the molecule is right-handed, with chiral axis along the  $z$  direction, and other parameters used here are provided in SI Appendix. The spin current polarization  $\sigma_s$  is oriented along the  $+z$  direction. Hence,  $V_y$  corresponds to the ISHE voltage and  $V_z$  corresponds to the ICISS voltage.

## **Supporting Information for**

# **Spin-to-charge conversion driven by inverse chiral-induced spin selectivity**

Tian-Yi Zhang<sup>1</sup>, Peng-Yi Liu<sup>1</sup>, Ai-Min Guo<sup>2</sup>, & Qing-Feng Sun<sup>1,3\*</sup>

\*Correspondence author: Qing-Feng Sun

Email: [sunqf@pku.edu.cn](mailto:sunqf@pku.edu.cn)

### **This PDF file includes:**

Supporting text  
Figures S1 to S2  
SI References

## Supporting Text

**Model Hamiltonian.** Based on the experimental configuration, we construct the Hamiltonian model describing the chiral molecular layer, the spin injector layer, and electrodes along the  $y$  and  $z$  directions. When probing the voltage  $V_y$  along the  $y$  direction, the Hamiltonian is  $H_{V_y} = H_{mol-layer} + H_{in} + H_y^{vol}$ , and when probing the voltage  $V_z$  along the  $z$  direction, the Hamiltonian is  $H_{V_z} = H_{mol-layer} + H_{in} + H_z^{vol}$ . Here,  $H_{mol-layer}$  is the Hamiltonian of the chiral molecular layer, and  $H_{in}$  is the Hamiltonian of the spin injector layer and its coupling to the chiral molecular layer.  $H_y^{vol}$  and  $H_z^{vol}$  describe the electrodes along  $y$  and  $z$  directions, respectively, as well as their coupling to the chiral molecular layer. In the following, we present systematically the specific forms of each Hamiltonian.

The Hamiltonian of chiral molecular layer is  $H_{mol-layer} = H_z^{mol} + H_{xy}^{mol} + H_{yz}^E$ , where  $H_z^{mol}$ ,  $H_{xy}^{mol}$  and  $H_{yz}^E$  describe the single nanofiber, electron hopping along the  $x$  and  $y$  directions, and SOC originating from the heterojunction, respectively. The chiral molecular layer is formed by stacking multiple nanofibers along the  $x$  and  $y$  directions. Each nanofiber consists of two intertwined helical single chains oriented along the  $z$ -axis, as shown in Fig. S2. The Hamiltonian for a single nanofiber is described by (1, 2):

$$H_z^{mol} = \sum_{n_x=1}^{L_x} \sum_{n_y=1}^{L_y} \sum_{n_z=1}^{L_z-1} \sum_{j=1}^2 \left[ t_1 c_{j,n_x,n_y,n_z}^\dagger c_{j,n_x,n_y,n_z+1} + i t_{so} c_{j,n_x,n_y,n_z}^\dagger (\sigma_{n_z}^{mol} + \sigma_{n_z+1}^{mol}) c_{j,n_x,n_y,n_z+1} + h.c. \right] \\ + \sum_{n_x=1}^{L_x} \sum_{n_y=1}^{L_y} \sum_{n_z=1}^{L_z} (t_2 c_{1,n_x,n_y,n_z}^\dagger c_{2,n_x,n_y,n_z} + h.c.), \quad [1]$$

where  $c_{j,n_x,n_y,n_z}^\dagger = (c_{j,n_x,n_y,n_z,\uparrow}^\dagger, c_{j,n_x,n_y,n_z,\downarrow}^\dagger)$  is the creation operator at site  $(n_x, n_y, n_z)$  of the  $j$ th chain, with  $n_x$ ,  $n_y$  and  $n_z$  labeling the monomers in the  $x$ ,  $y$  and  $z$  direction. This layer has thickness  $L_x$ , width  $L_y$ , and each molecule has a length  $L_z$ . “ $h.c.$ ” represents the Hermitian conjugation.  $t_1$  is the intra-chain hopping integral,  $t_2$  is the inter-chain hopping integral, and  $t_{so}$  is the intrinsic molecular SOC.  $\sigma_{n_z+1}^{mol} = \sigma_x \sin(n_z \Delta\varphi) \sin \theta_{mol} - \sigma_y \cos(n_z \Delta\varphi) \sin \theta_{mol} + \sigma_z \cos \theta_{mol}$ , where  $\sigma_{x,y,z}$  are the Pauli matrices.  $\theta_{mol} = \arctan[h/(2\pi R)]$  is the helix angle of molecule with helical pitch  $h$  and helical radius  $R$ , and  $\Delta\varphi$  is the twist angle between neighboring sites. The first term in  $H_z^{mol}$  describes the “through-bond” motion of electrons along each helical single chain (3, 4), encompassing both spin-independent hopping  $t_1$  and SOC  $t_{so}$ . This Hamiltonian is obtained through the same discretization procedure as in our previous works (1, 2, 5, 6), and maintaining formal consistency. The second term in  $H_z^{mol}$  describes the “chain-to-chain” hopping between the two intertwined chains (3, 4) (see Fig. S2). Due to the close proximity of the chains (as illustrated in Fig. 1 and Fig. S2), only the nearest-neighbor hopping  $t_2$  between adjacent sites is considered.

The inter-nanofiber hopping of electrons along the  $x$  and  $y$  directions (3, 4) is described by the Hamiltonian  $H_{xy}^{mol}$ :

$$H_{xy}^{mol} = \sum_{n_x=1}^{L_x-1} \sum_{n_y=1}^{L_y} \sum_{n_z=1}^{L_z} \sum_{j=1}^2 \left( t_2 c_{j,n_x,n_y,n_z}^\dagger c_{j,n_x+1,n_y,n_z} + h.c. \right) \\ + \sum_{n_x=1}^{L_x} \sum_{n_y=1}^{L_y-1} \sum_{n_z=1}^{L_z} \sum_{j=1}^2 \left( t_2 c_{j,n_x,n_y,n_z}^\dagger c_{j,n_x,n_y+1,n_z} + h.c. \right). \quad [2]$$

The first term in  $H_{xy}^{mol}$  describes the inter-nanofiber hopping of electrons in the  $x$  direction, while the second term in  $H_{xy}^{mol}$  describes the inter-nanofiber hopping in the  $y$  direction, as shown in Fig. S2. In the experiment, the distance between adjacent helical nanofiber is small, and the magnitude of inter-nanofiber hopping decreases exponentially rapidly with distance. Therefore, only the nearest-neighbor inter-nanofiber hopping perpendicular to the helical axis direction is considered here.

The SOC induced by the electric field parallel to the  $x$  axis, originating from the heterojunction, is described by the Hamiltonian  $H_{yz}^E$ :

$$H_{yz}^E = \sum_{n_x=1}^{L_x} \sum_{n_y=1}^{L_y} \sum_{n_z=1}^{L_z-1} \sum_{j=1}^2 \left[ it_{so}^E c_{j,n_x,n_y,n_z}^\dagger (\sigma_{n_z}^E + \sigma_{n_z+1}^E) c_{j,n_x,n_y,n_z+1} + h.c. \right] \\ + \sum_{n_x=1}^{L_x} \sum_{n_y=1}^{L_y} \sum_{n_z=1}^{L_z} (-2it_{so}^E c_{1,n_x,n_y,n_z}^\dagger \sigma_y c_{2,n_x,n_y,n_z} + h.c.) \\ + \sum_{n_x=1}^{L_x} \sum_{n_y=1}^{L_y-1} \sum_{n_z=1}^{L_z} \sum_{j=1}^2 \left( 2it_{so}^E c_{j,n_x,n_y,n_z}^\dagger \sigma_z c_{j,n_x,n_y+1,n_z} + h.c. \right), \quad [3]$$

where  $t_{so}^E$  represents the corresponding SOC strength, and  $\sigma_{n_z+1}^E = -\sigma_y \sin \theta_{mol} + \sigma_z \cos(n_z \Delta \varphi) \cos \theta_{mol}$ . This Hamiltonian is obtained by discretizing  $H_{so}^E = e\hbar/(4m_e^2 c^2) [\mathbf{E}_x \cdot (\boldsymbol{\sigma} \times \mathbf{p})]$ , following the same procedure applied to the chiral molecules (1, 2, 6). The first term in this Hamiltonian describes the SOC experienced by electrons moving within a single chain due to the heterojunction's electric field (7, 8). The second term describes the SOC experienced by electrons moving between the two chains within the same nanofiber. The third term describes the SOC experienced by electrons during inter-nanofiber movement along the  $y$  direction.

The Hamiltonian of the chiral molecular layer  $H_{mol-layer}$  preserves the electron-hole symmetry (9), i.e.  $H_{mol-layer}$  remains invariant under the transformation  $c_{j,n_x,n_y,n_z,\uparrow} \rightarrow (-1)^{j+n_x+n_y+n_z} c_{j,n_x,n_y,n_z,\downarrow}^\dagger, c_{j,n_x,n_y,n_z,\downarrow} \rightarrow (-1)^{j+n_x+n_y+n_z+1} c_{j,n_x,n_y,n_z,\uparrow}^\dagger$ . This property leads to  $V_y(-E) = -V_y(E)$ , and  $V_z(-E) = -V_z(E)$  in Fig. 2.

When disorder is taken into account, the Hamiltonian needs to add an additional term (10):  $H_{dis} = \sum_{n_x=1}^{L_x} \sum_{n_y=1}^{L_y} \sum_{n_z=1}^{L_z} \sum_{j=1}^2 w_{j,n_x,n_y,n_z} c_{j,n_x,n_y,n_z}^\dagger c_{j,n_x,n_y,n_z}$ , where the on-site disorder energy  $w_{j,n_x,n_y,n_z}$  is uniformly distributed in the range  $[-W/2, W/2]$  with the disorder strength  $W$ .

The Hamiltonian of the spin injector layer and its coupling to the chiral molecular layer is described by  $H_{in}$ :

$$\begin{aligned}
H_{in} = & \sum_{n_x > L_x} \sum_{n_y=1}^{L_y} \sum_{n_z=1}^{L_z} \sum_{j=1}^2 \left( t_2 a_{j,n_x,n_y,n_z}^\dagger a_{j,n_x+1,n_y,n_z} + h.c. \right) \\
& + \sum_{n_x > L_x} \sum_{n_y=1}^{L_y-1} \sum_{n_z=1}^{L_z} \sum_{j=1}^2 \left( t_2 a_{j,n_x,n_y,n_z}^\dagger a_{j,n_x,n_y+1,n_z} + h.c. \right) \\
& + \sum_{n_x > L_x} \sum_{n_y=1}^{L_y} \sum_{n_z=1}^{L_z-1} \sum_{j=1}^2 \left( t_1 a_{j,n_x,n_y,n_z}^\dagger a_{j,n_x,n_y,n_z+1} + h.c. \right) \\
& + \sum_{n_x > L_x} \sum_{n_y=1}^{L_y} \sum_{n_z=1}^{L_z} \left( t_2 a_{1,n_x,n_y,n_z}^\dagger a_{2,n_x,n_y,n_z} + h.c. \right) \\
& + \sum_{n_y=1}^{L_y} \sum_{n_z=1}^{L_z} \sum_{j=1}^2 \left( t_2 a_{j,L_x+1,n_y,n_z}^\dagger c_{j,L_x,n_y,n_z} + h.c. \right), \quad [4]
\end{aligned}$$

where  $a_{j,n_x,n_y,n_z}^\dagger = (a_{j,n_x,n_y,n_z,\uparrow}^\dagger, a_{j,n_x,n_y,n_z,\downarrow}^\dagger)$  is the creation operator in the spin injector layer. This Hamiltonian describes the semi-infinite spin injector layer (and thus can be regarded as an electrode) and its coupling with the molecular layer. Due to the small magnitude of the external magnetic field in the experiment (11) (up to 50 mT, corresponding to an electron energy level splitting of approximately 0.006 meV), its primary effect is merely to alter the spin bias in the spin injector layer (see the Transport Formulation section). Consequently, within the system, we only consider the influence of the spin bias and neglect other effects arising from the applied magnetic field.

The Hamiltonians describing the semi-infinite measurement electrodes and their couplings to the chiral molecular layer along the  $y$  and  $z$  directions, respectively, are given by:

$$H_y^{vol} = \sum_{k_y, \beta (\beta=+y, -y)} \sum_{n_x=1}^{L_x} \sum_{n_z=1}^{L_z} \sum_{j=1}^2 \left( \varepsilon_{k_y, \beta} b_{j,n_x,k_y,n_z, \beta}^\dagger b_{j,n_x,k_y,n_z, \beta} + \tau b_{j,n_x,k_y,n_z, \beta}^\dagger c_{j,n_x,n_y, \beta, n_z} + h.c. \right), \quad [5]$$

$$H_z^{vol} = \sum_{k_z, \beta (\beta=+z, -z)} \sum_{n_x=1}^{L_x} \sum_{n_y=1}^{L_y} \sum_{j=1}^2 \left( \varepsilon_{k_z, \beta} b_{j,n_x,n_y,k_z, \beta}^\dagger b_{j,n_x,n_y,k_z, \beta} + \tau b_{j,n_x,n_y,k_z, \beta}^\dagger c_{j,n_x,n_y,n_z, \beta} + h.c. \right), \quad [6]$$

where  $b_{j,n_x,k_y,n_z, \beta}^\dagger = (b_{j,n_x,k_y,n_z, \beta, \uparrow}^\dagger, b_{j,n_x,k_y,n_z, \beta, \downarrow}^\dagger)$  and  $b_{j,n_x,n_y,k_z, \beta}^\dagger = (b_{j,n_x,n_y,k_z, \beta, \uparrow}^\dagger, b_{j,n_x,n_y,k_z, \beta, \downarrow}^\dagger)$  are the creation operators in the voltage probe, with  $n_{y,-y} = 1, n_{y,+y} = L_y, n_{z,-z} = 1, n_{z,+z} = L_z$ .

**Transport formulation.** The voltage measurement configurations along the  $y$  and  $z$  directions are calculated similarly using the non-equilibrium Green's function method. In the following we label the electrodes with  $p$ , following convention:

1. For the  $y$  direction voltage measurement, the Hamiltonian is  $H_{V_y} = H_{mol-layer} + H_{in} + H_y^{vol}$ . The labels are  $p = in, +y, -y$ , corresponding to the electrodes described by Eq. (4) (for  $p = in$ ) and Eq. (5) (for  $p = \pm y$ ).

2. For the  $z$  direction voltage measurement, the Hamiltonian is  $H_{V_z} = H_{mol-layer} + H_{in} + H_z^{vol}$ . The labels are  $p = in, +z, -z$ , corresponding to the electrodes described by Eq. (4) (for  $p = in$ ) and Eq. (6) (for  $p = \pm z$ ).

According to the Landauer-Büttiker formula (12), the current with spin  $s = \uparrow, \downarrow$  from electrode  $p$  to the chiral molecular layer is given by:

$$I_{ps} = \frac{e^2}{h} \sum_{qs'} T_{ps,qs'} (V_{ps} - V_{qs'}) \quad [7]$$

where  $T_{ps,qs'} = \text{Tr}[\Gamma_{ps'} \mathbf{G}^r \Gamma_{qs'} \mathbf{G}^a]$  is the transmission coefficient from electrode  $q$  with spin  $s'$  to the electrode  $p$  with spin  $s$ . The retarded Green's function  $\mathbf{G}^r = [\mathbf{G}^a]^\dagger = [E\mathbf{I} - \mathbf{H}_{mol-layer} - \Sigma_{ps}^r]^{-1}$ , the linewidth function  $\Gamma_{ps} = i[\Sigma_{ps}^r - \Sigma_{ps}^a]$ , and  $\mathbf{I}$  is the identity matrix. The bold letters represent the matrix under the tight-binding representation.  $E$  is the Fermi energy,  $\Sigma_{ps}^r = [\Sigma_{ps}^a]^\dagger$  is the retarded self-energy due to the coupling to the electrode  $p$  with spin  $s$ . For the spin injector layer, the self-energy of spin- $s$  (in arbitrary direction) can be calculated numerically (8, 13). For the electrodes along the  $y$  and  $z$  directions,  $\Sigma_{ps}^r = -i\Gamma_p/2 = -i\pi\rho_p\tau^2$  is energy independent, with  $\rho_p$  being the density of states in  $p$  electrode, and  $\Gamma_p$  the linewidth parameter (1).

Considering the Fermi energy splitting of different spins in the spin injector layer, the spin voltage is obtained as  $V_{in,-s} = -V_{in,s}$ . For the voltage probes in the  $y$  and  $z$  directions,  $V_{p\downarrow} = V_{p\uparrow}$ . Since there is no net charge current for these voltage probes, we have  $I_{p\uparrow} + I_{p\downarrow} = 0$ . Under these boundary conditions, the current and voltage at each electrode can be derived using Eq. (8), and the measured voltage is given by  $V_y = V_{+y} - V_{-y}$  and  $V_z = V_{+z} - V_{-z}$ .

**Model parameters.** Within the chiral molecular layer, experimental measurements show identical carrier mobility parallel and perpendicular to the chiral axis  $\mathbf{\Omega}_{R/S}$  (11). This indicates equivalent intra-nanofiber and inter-nanofiber hopping energies (12). Therefore, we set  $t_1 = t_2$  and take  $t_1$  as the energy unit. The structural parameters of single helical chain adapted from the experiment (11, 14) are the radius  $R = 10$  nm, and the helical pitch  $h = 40$  nm. The twist angle is chosen as  $\Delta\varphi = \pi/12$ . Limited by computational resources (the entire system is three-dimensional), we simulate a system of relatively small size:  $L_x = 4, L_y = 25, L_z = 25$ . To compensate for the reduced spin conversion capability inherent to this smaller size, we select relatively large SOC strengths:  $t_{so} = 0.1t_1, t_{so}^E = 0.05t_1$ . As shown in Fig. 4, the voltages associated with the ISHE and the ICIS increase with larger material size. Consequently, the larger the actual dimensions, the smaller the required SOC (15), and our computational results effectively correspond to physically larger

systems with smaller SOC. For the voltage probes along the  $y$  and  $z$  directions, the linewidth parameters are fixed as  $\Gamma_{+y} = \Gamma_{-y} = \Gamma_{+z} = \Gamma_{-z} = t_1$ . The strength of disorder  $W = t_1$ , and we calculate and statistically analyze the results for 1000 different disorder configurations (see Fig. S1). The voltages of spin injector layer are set as  $V_{in,\uparrow} = -V_{in,\downarrow} = V_0$ . The above-mentioned values of parameters are used throughout this paper except for specific indications in the figure.

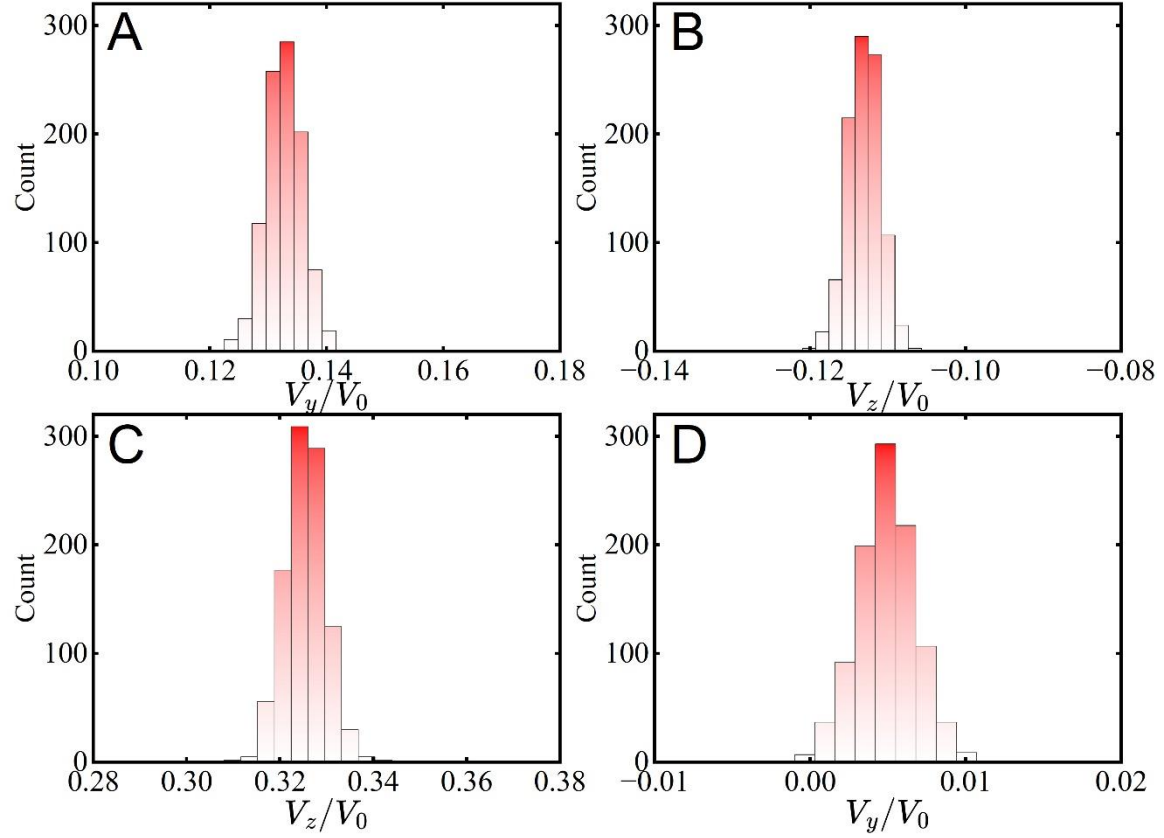


**Fig. S1.** The influence of disorder on ISHE and ICISS. (A-B) Effect of disorder on ISHE along the  $y$  (A) and  $z$  (B) directions. (C-D) Effect of disorder on ICISS along the  $z$  (C) and  $y$  (D) directions. For each panel (A-D), the figure presents the statistical distribution of the voltage magnitude at energy  $E = -4t_1$  for right-handed molecules across 1000 different disorder configurations. The disorder strength is  $W = t_1$ . All other parameters are identical to those used in Fig. 2 of the main text.

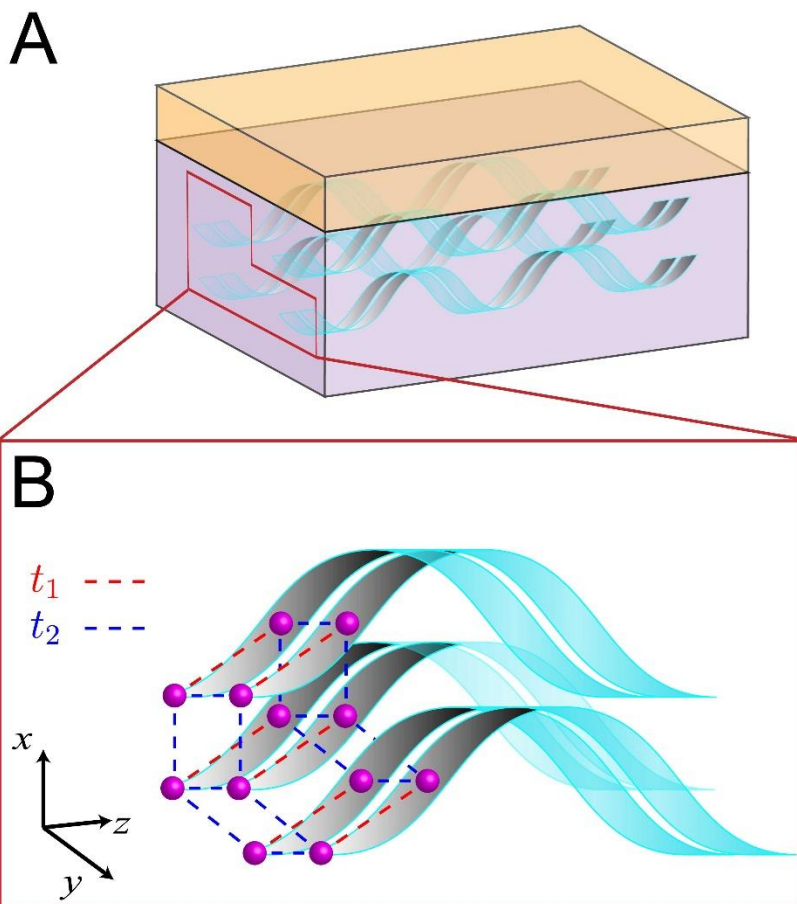


**Fig. S2.** Schematic diagram of the chiral molecular layer model. (A) Schematic diagram of the experimental configuration, where orange and purple boxes represent the spin current injector layer and the chiral molecular layer, respectively. (B) Schematic diagram of the chiral molecules and hopping. Purple spheres represent the monomers on each chiral chain. Red dashed lines and blue dashed lines represent the intra-chain hopping ( $t_1$ ) and inter-nanofiber hopping ( $t_2$ ) of electrons, respectively. Here the spacing between monomers and between nanofibers is exaggerated in the diagram for clarity.

## SI References

1. A.-M. Guo, Q.-F. Sun, Spin-Selective Transport of Electrons in DNA Double Helix. *Phys. Rev. Lett.* 108, 218102 (2012).
2. A.-M. Guo, Q.-F. Sun, Spin-dependent electron transport in protein-like single-helical molecules. *Proc. Natl. Acad. Sci. U.S.A.* 111, 11658–11662 (2014).
3. H. Song, H. Lee, T. Lee, Intermolecular Chain-to-Chain Tunneling in Metal–Alkanethiol–Metal Junctions. *J. Am. Chem. Soc.* 129, 3806–3807 (2007).
4. T. Frederiksen, et al., Exploring the Tilt-Angle Dependence of Electron Tunneling across Molecular Junctions of Self-Assembled Alkanethiols. *ACS Nano* 3, 2073–2080 (2009).
5. T.-Y. Zhang, Y. Mao, A.-M. Guo, Q.-F. Sun, Dynamical theory of chiral-induced spin selectivity in electron donor–chiral molecule–acceptor systems. *Phys. Rev. B* 111, 205417 (2025).
6. C. Wang, et al., Transverse Spin Selectivity in Helical Nanofibers Prepared without Any Chiral Molecule. *Phys. Rev. Lett.* 133, 108001 (2024).
7. Y. A. Bychkov, E. I. Rashba, Oscillatory effects and the magnetic susceptibility of carriers in inversion layers. *J. Phys. C: Solid State Phys.* 17, 6039–6045 (1984).
8. Y. Xing, Q.-F. Sun, J. Wang, Symmetry and transport property of spin current induced spin-Hall effect. *Phys. Rev. B* 75, 075324 (2007).
9. T.-R. Pan, A.-M. Guo, Q.-F. Sun, Spin-polarized electron transport through helicene molecular junctions. *Phys. Rev. B* 94, 235448 (2016).
10. W. Long, Q.-F. Sun, J. Wang, Disorder-Induced Enhancement of Transport through Graphene p – n Junctions. *Phys. Rev. Lett.* 101, 166806 (2008).
11. R. Sun, et al., Inverse chirality-induced spin selectivity effect in chiral assemblies of  $\pi$ -conjugated polymers. *Nat. Mater.* 23, 782–789 (2024).
12. S. Datta, *Electronic Transport in Mesoscopic Systems*, 1st Ed. (Cambridge University Press, 1995).
13. D. H. Lee, J. D. Joannopoulos, Simple scheme for surface-band calculations. I. *Phys. Rev. B* 23, 4988–4996 (1981).
14. K. S. Park, et al., Chiral emergence in multistep hierarchical assembly of achiral conjugated polymers. *Nat Commun* 13, 2738 (2022).
15. Q.-F. Sun, J. Wang, H. Guo, Quantum transport theory for nanostructures with Rashba spin-orbital interaction. *Phys. Rev. B* 71, 165310 (2005).